



Ball-flower like NiO/g-C₃N₄ heterojunction for efficient visible light photocatalytic CO₂ reduction

Jun-ying Tang^a, Rui-tang Guo^{b,c,d,✉*}, Wei-guo Zhou^{a,d,✉*}, Chun-ying Huang^{b,c}, Wei-guo Pan^{b,c,*}

^a College of Mechanical Engineering, Tongji University, Shanghai, China

^b College of Energy and Mechanical Engineering, Shanghai University of Electric Power, Shanghai, China

^c Shanghai Engineering Research Center of Power Generation Environment Protection, Shanghai, China

^d Shanghai Institute of Pollution Control and Ecological Security, Shanghai, 200092, China



ARTICLE INFO

Keywords:

g-C₃N₄
NiO/g-C₃N₄ composite
p-n heterojunction
CO₂ photoreduction
Ball-flower

ABSTRACT

A ball-flower like NiO/g-C₃N₄ heterojunction composite was synthesized via a hydrothermal deposition method combined with subsequent calcination route. The NiO/g-C₃N₄ heterojunction exhibited a superior performance in CO₂ photoreduction. A maximum CO yields of 4.17 μmol/(h g-cat) had been obtained on 40% NiO/g-C₃N₄ composite, which was 2.5 and 7.6 times as high as the pure g-C₃N₄ and NiO respectively. The promotion mechanism could be ascribed to the perfect band matching and efficient internal charge transfer within the p-n junction, which results in high-efficiency separation of photogenerated electron-hole pairs, strong visible-light response and high specific surface area.

1. Introduction

With the consumption of energy and the aggravation of global environmental contamination, reduction CO₂ into hydrocarbons is one of the potential solutions to alleviate the energy crisis and gain environmental improvements [1,2]. One potential way is to reduce carbon dioxide to methane by light-driven photocatalysts with water [3,4]. Since the graphitic carbon nitride (g-C₃N₄) was firstly proposed for photocatalytic H₂ production, g-C₃N₄ has been extensively investigated due to its good chemical stability, easy availability, attractive electronic structure and environmental friendliness [5,6]. Nevertheless, applying pristine g-C₃N₄ still suffers from some obstacles, such as high recombination rate of photogenerated carriers, low electroconductibility, inefficient solar utilization as well as low quantum efficiency [7–9]. In order to overcome these weakness, various strategies have been attempted such as metal and nonmetal modification [10–13], texture fabrication [14,15] and the heterojunction formation by combining it with other suitable catalysts [16–20]. Among them, establishing p-n junction at the interface between the n-type g-C₃N₄ and the p-type semiconductor has been considered as a potential way to enhance the photocatalytic activity, in which the internal electric field could acts as a potential barrier to decrease the electron–hole pairs recombination [21].

NiO, as a p-type semiconductor, possesses super hole mobility, high

cost-effectiveness and high lattice match with g-C₃N₄. It has been used as a popular hole transport material for dye sensitized solar cells [22–24] and thin film photovoltaics [25]. Moreover, it has acted as an efficient co-catalyst for water splitting to produce H₂ [26,27]. When it contacts with water during the hydrogen production, the NiO forms a band that is bent to lead photogenerated electrons into the aqueous phase. Meanwhile, the chemisorbed oxygen could incorporate into the NiO lattice and generate Ni³⁺ ions and cationic vacancies and the Ni²⁺ vacancies in NiO created by the formed Ni³⁺ could reduce the electric resistance of NiO, which is favorable to the decrease of the recombination rate [27,28]. However, NiO has a poor photocatalytic activity due to the low concentration of Ni³⁺ in it [29–31]. In addition, the wide band gap also precludes its visible light adsorption. Therefore, some researchers have tried to couple NiO with a synergic dopant such as n-type semiconductors to increase the lifetime of photoelectric electrons and extend the light adsorption. For example, TiO₂-NiO p-n junction was widely used in photocatalytic degradation [32,33] and photocatalytic evolution of hydrogen [34]. The p-n heterojunction can produce more efficient electrons to participate in the reaction. Lu et al. [35] synthesized NiO-ZnO p-n junction by the template-assisted approach. The heterojunction prevented the electron–hole recombination and consequently improved its photocatalytic degradation activity. A hierarchical three dimensional (3D) NiO–CdS heteroarchitecture exhibited great photocatalytic activity for hydrogen generation with 6%

* Corresponding author at: College of Energy and Mechanical Engineering, Shanghai University of Electric Power, Shanghai, China.

** Corresponding authors at: Shanghai Institute of Pollution Control and Ecological Security, Shanghai, 200092, China.

E-mail addresses: grta@zju.edu.cn (R.-t. Guo), tjweiguo@tongji.edu.cn (W.-g. Zhou), pweiguo@163.com (W.-g. Pan).

apparent quantum yields (AQY) value, which was mainly arised from to the facile charge transfer in heteroarchitecture and the extended light adsorption edge [36]. NiO has been deemed to be an appropriate photocatalyst to form a p–n junction [37].

Encouraged by the above concept and inference, it is speculated that combining NiO and g-C₃N₄ into a heteroarchitecture could be achieved via mutual activation between them. The electron–hole recombination can be efficiently suppressed within the p–n junction. However, to our best knowledge, the hybrid NiO/g-C₃N₄ photocatalyst is rarely applied in photocatalytic reaction [38], and the utilization of NiO/g-C₃N₄ heterojunction in CO₂ photoreduction has never been reported. Therefore, in the present work, we synthesized a ball-flower like NiO/g-C₃N₄ heterojunction by a hydrothermal process combined with the subsequent calcination route. The hybrids exhibited excellent performance in photoreduction of CO₂ with H₂O under visible-light irradiation. Moreover, the surface morphological structure, structural properties, optical and photoelectrochemical characteristics of the NiO/g-C₃N₄ composites were studied and discussed in detail.

2. Experimental

2.1. Synthesis

The g-C₃N₄ was prepared by a facile method: a quantity of urea was annealed at 520 °C in air for 4 h. After that, the g-C₃N₄ catalyst with a light yellow color was obtained and milled for standby application.

The NiO/g-C₃N₄ heterojunction composites with different mass ratios of NiO (0, 20, 40, 60 and 80 wt%) were obtained by the following process: 0.5 g g-C₃N₄ was added in 60 ml ethanol and then ultrasonic dispersion for 30 min. Subsequently, a certain amount (0, 0.389, 0.778, 1.168 and 1.557 g) of Ni(NO₃)₂·6H₂O and urea (1 g) were dissolved in the solution and stirred vigorously for 30 min. Then the solution was treated with a hydrothermal route at 180 °C for 12 h. The resulted products were washed with deionized water and dried at 80 °C. Next then, the NiO/g-C₃N₄ composites with a dark-green color were obtained by calcining the hydrothermal products in air at 380 °C for 2 h. The pure NiO was obtained by the same method but without the g-C₃N₄ addition.

2.2. Characterization

The surface characteristic of the catalysts were observed by a scanning electron microscopy (SEM, Phillips XL-30 FEG/NEW) and a transmission electron microscopy (TEM, Phillips Model CM200). The crystal phase of the catalysts was analyzed by powder X-ray diffraction patterns (XRD) on a Bruker D8 diffractometer with Cu K α radiation. The measurement was conducted in the 2 θ range of 10–80°. The functional groups were characterized by Fourier transform infrared (FT-IR) spectrum (Nicolet iS50). X-ray photoelectron spectroscopy (XPS, ESCALAB 250xi, USA) with Al K α radiation source was used to analyze the surface chemical compositions and valance band (VB) spectra. N₂ adsorption–desorption measurement was conducted at 77 K to analyze the specific surface area and pore structure (Quantachrome Autosorb-iQ-AG instrument). To analyze the optical properties, ultraviolet visible (UV-vis) diffuse reflection spectra and photoluminescence (PL) spectra were analyzed on a spectrophotometer (SHIMADZU UV-3600, Japan) and fluorescence spectrophotometer (Hitachi F-4600) with an excitation wavelength of 325 nm.

2.3. Photoelectrochemical measurements

Photoelectrochemical measurements were performed on an electrochemical system (CHI 660E, Shanghai Chenhua Instrument Co. Ltd. China) with a standard three-electrode system in a 0.5 M Na₂SO₄ electrolyte solution. The FTO glass coated with the prepared photocatalyst was used as the working electrode while Ag/AgCl and Pt electrodes were served as the reference and the counter electrode,

respectively. The working electrode was obtained as follows: 10 mg prepared photocatalyst was dispersed in 1 mL ethanol and 20 μ L nafion aqueous solution (5 wt%), and then ultrasonically scattered for 2 h. In succession, 0.1 mL slurry was added dropwise on the FTO glass (1 × 1 cm), and the photocatalyst was attached on the FTO glass surface after the ethanol evaporated. The Mott–Schottky measurement was performed at two frequencies of 500 Hz and 1000 Hz respectively. Photocurrent and electrochemical impedance (EIS) tests were carried out using a 300 W Xenon-lamp.

2.4. Photocatalytic activity evaluation

The activity of CO₂ photocatalytic reduction was tested in a gas-closed circulation system with a 500 mL reactor (Perfect Light Company, Beijing, China). The reaction was performed with a 300 W Xenon-arc lamp as a light source. In general, the solution contained 50 mg photocatalyst and 100 mL deionized water were stirred continuously, and then the suspension was vacuum-treated and filled with 100 kPa CO₂ (99.999%) for 30 min to reach the adsorption–desorption equilibrium before illumination. The experiment was started when the light was on. The reactor temperature were maintained at 25 °C via a cooling sink. During the reaction, the products were quantified per hour by a gas chromatograph (GC-2010 Plus, SHIMADZU, Japan).

3. Results and discussion

The SEM images of pure g-C₃N₄, pure NiO and NiO/g-C₃N₄ heterojunction samples are shown in Fig. 1. It can be observed that pure g-C₃N₄ presents a two-dimensional (2D) lamellar structure (Fig. 1a) while the pure NiO exhibits perfect ball-flower morphology (Fig. 1b). The SEM image and corresponding elemental mapping images of 40% NiO/g-C₃N₄ sample are shown in Fig. 1c, it can be detected that the composite inherits the morphology of both NiO and g-C₃N₄, implying a ball-flower structure with curly and irregular shape feathered edge. Furthermore, the corresponding mapping images reveal the coexistence of C, N, O and Ni elements in the NiO/g-C₃N₄ catalyst.

The XRD patterns of the synthesized catalysts were recorded to identify their crystal phases. As observed in Fig. 2a, the peak at 27.5° in the g-C₃N₄ is the characteristic (002) plane peak arising from the interlayer stacking of aromatic planes in the g-C₃N₄. The peak at 13.1° could be assigned to the (100) plane, representing the in-plane structure packing motif of tri-s-triazine units [39]. The prepared NiO presents five main peaks at $2\theta = 37.2^\circ$, 43.3° , 62.9° , 75.4° and 79.4° corresponding to the (111), (200), (220), (311) and (222) planes, respectively, which is in accordance with the Powder Diffraction Standards data (JCPDS PDF# 47–1049). All diffraction peaks of NiO and g-C₃N₄ are observed clearly in NiO/g-C₃N₄ composites, suggesting the coexistence of NiO and g-C₃N₄. Noticeably, with the increase of NiO content in the composites, the peak intensity of g-C₃N₄ becomes weaker, whereas the diffraction peaks of NiO becomes stronger. To further research the functional groups of the photocatalysts, FT-IR analysis was performed and the spectra are illustrated in Fig. 2b. It is clearly observed three main characteristic peaks in pure g-C₃N₄. The broad peaks ranging from 3000 to 3600 cm⁻¹ are associated with the stretching vibration of N–H or O–H of H₂O [40]. The skeletal adsorption bands of 1200–1700 cm⁻¹ belong to the typical stretching modes of CN heterocycles [41]. Besides, the peak at 812 cm⁻¹ is ascribed to the breathing mode of tri-azine units [42]. In the case of NiO, the broad adsorption bands at around 428 cm⁻¹ and 1652 cm⁻¹ are assigned to the Ni–O vibration adsorption and O–H stretching deformation [43], while the broad adsorption region with the maximum peak at around 3465 cm⁻¹ should be originated from the hydroxyl groups and absorbed water [44]. Furthermore, all characteristic peaks of both g-C₃N₄ and NiO can be observed in NiO/g-C₃N₄ composite samples, and the Ni–O peak intensity increases with increasing NiO amount. It is noteworthy that the peak observed at 428 cm⁻¹ in NiO spectra shifts to

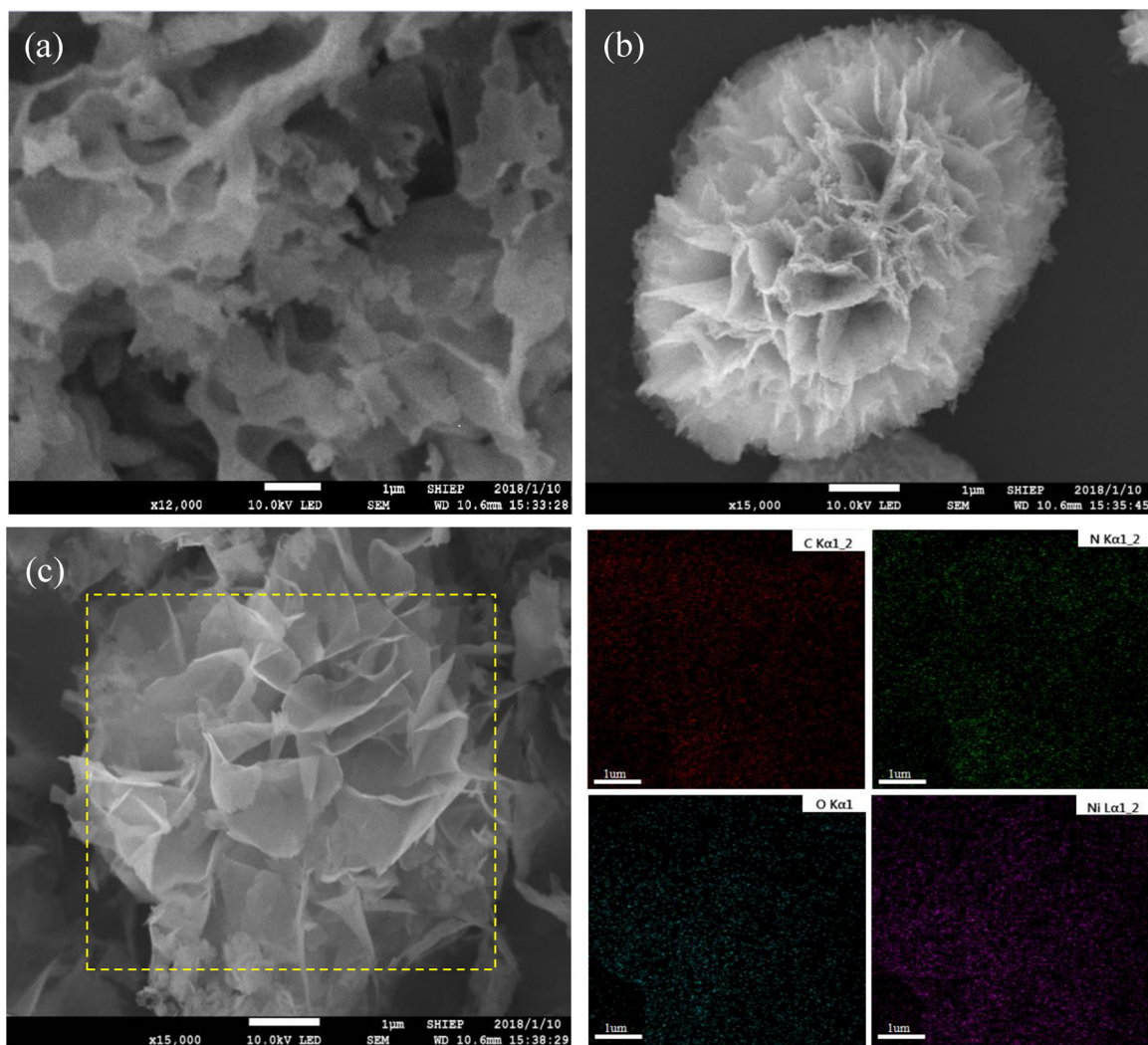


Fig. 1. (a) SEM image of pure g-C₃N₄; (b) SEM image of pure NiO; (c) SEM image and corresponding elemental mapping images of C, N, Ni, O in 40% NiO/g-C₃N₄ sample.

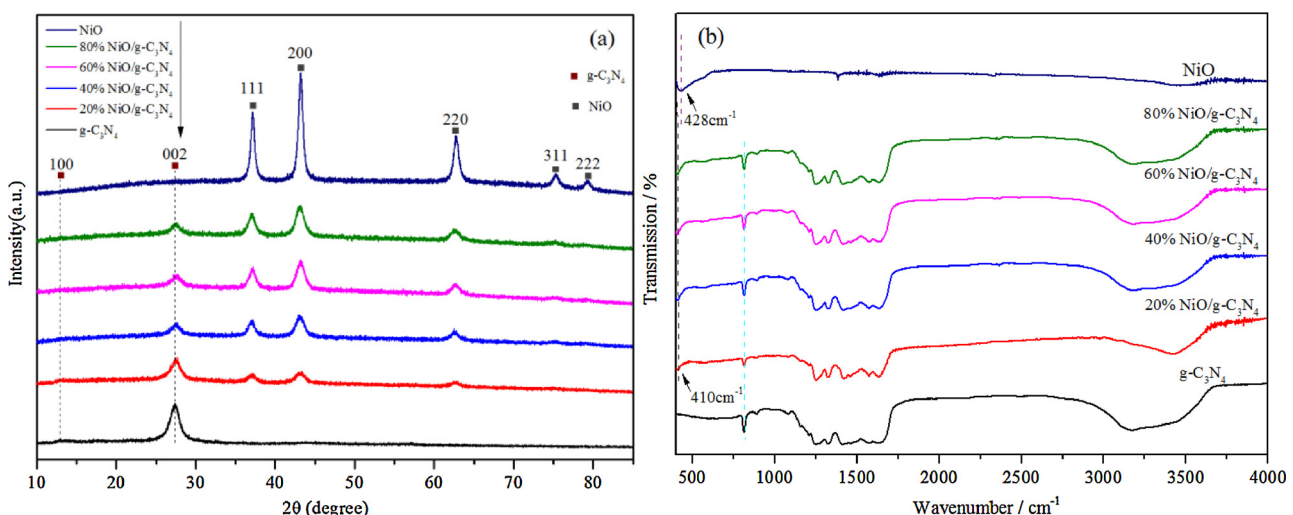


Fig. 2. (a) XRD patterns and (b) FT-IR spectra of pure g-C₃N₄, pure NiO and NiO/g-C₃N₄ composites.

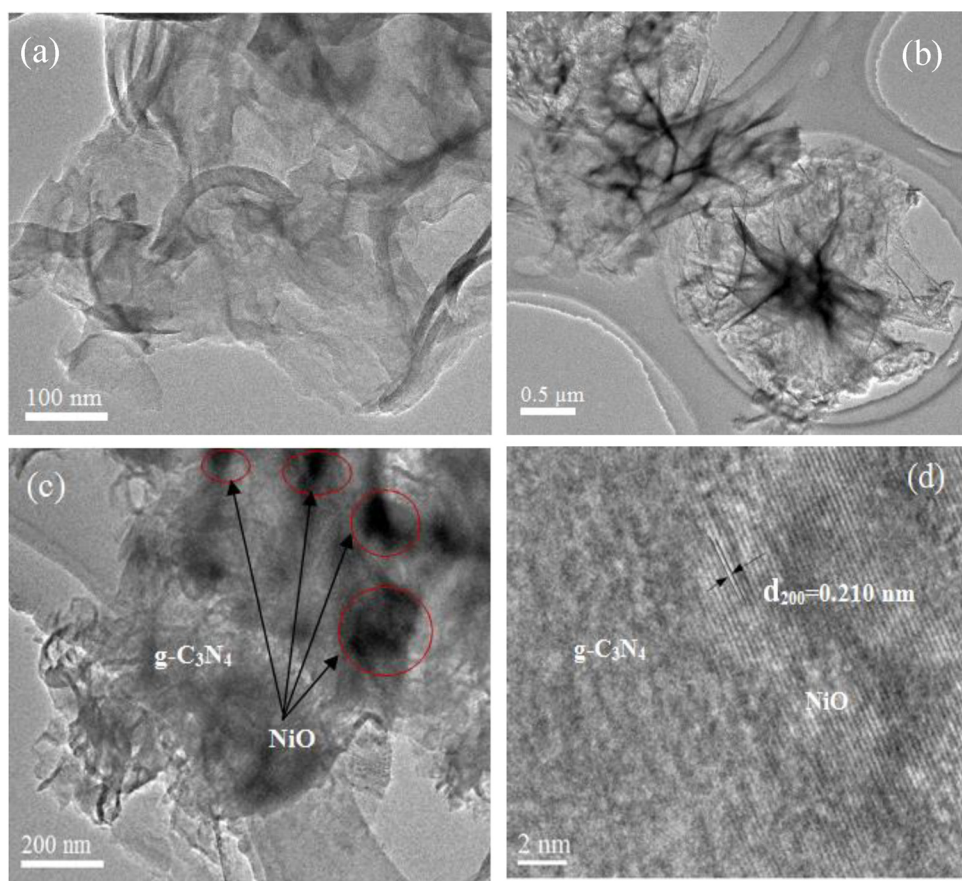


Fig. 3. TEM image of (a) pure $\text{g-C}_3\text{N}_4$, (b) NiO and (c) 40% NiO/ $\text{g-C}_3\text{N}_4$; (d) HRTEM of 40% NiO/ $\text{g-C}_3\text{N}_4$ sample.

410 cm^{-1} in NiO/ $\text{g-C}_3\text{N}_4$ composites, which suggests the hydroxyl groups and triazine rings of $\text{g-C}_3\text{N}_4$ are successfully interacted with NiO via hydrogen bonding or electrostatic interaction. The XRD and FT-IR results manifest the NiO/ $\text{g-C}_3\text{N}_4$ p-n junctions were formed expectedly.

A high-resolution TEM (HRTEM) image is shown in Fig. 3. Fig. 3a and b shows the microscopic morphology of pure $\text{g-C}_3\text{N}_4$ and NiO, which clearly demonstrates the flaky structure with curly edge and ball-flower morphologies with transparent and smooth edge, respectively, which is in good accordance with the SEM images depicted above. The TEM image of 40% NiO/ $\text{g-C}_3\text{N}_4$ sample reveals the NiO and $\text{g-C}_3\text{N}_4$ are combined together uniformly (Fig. 3c). Moreover, a 0.210 nm interplanar spacing is clearly observed in Fig. 3d, corresponding to the (200) crystal plane of cubic-structured NiO [45]. The results suggest the p-n junction has been formed in the ball-flower like 40% NiO/ $\text{g-C}_3\text{N}_4$ composite.

Surface chemical compositions of the pure $\text{g-C}_3\text{N}_4$, pure NiO and 40% NiO/ $\text{g-C}_3\text{N}_4$ heterostructure were further studied by XPS. As shown in the survey scan XPS spectrum (Fig. 4a), C 1s and N 1s are detected in $\text{g-C}_3\text{N}_4$, NiO and 40% NiO/ $\text{g-C}_3\text{N}_4$, while Ni 2p and O 1s peaks are observed in the spectra of NiO and 40% NiO/ $\text{g-C}_3\text{N}_4$. It is noted that the carbon detected in pure NiO may be caused by the adventitious carbon. The existence of Ni in 40% NiO/ $\text{g-C}_3\text{N}_4$ composite implies the incorporation of NiO into $\text{g-C}_3\text{N}_4$ successfully. The corresponding high-resolution spectra of C1s, N 1s, O 1s and Ni 2p are also shown in Fig. 4. Two sub-bands located at 284.8 and 288.1 eV (Fig. 4b) can be observed in C 1s spectra of the $\text{g-C}_3\text{N}_4$, which corresponds to C–C bond and N=C=N group, respectively [46]. Fig. 4c shows the N1s spectra for both $\text{g-C}_3\text{N}_4$ and NiO/ $\text{g-C}_3\text{N}_4$. The dominated peak at 398.6 eV belongs to sp^2 hybridized aromatic N bonded to carbon (C=N–C) [47], while the peak at 399.8 eV and 404.2 eV are ascribed to the tertiary nitrogen N–(C)₃ groups and π excitations [48]. The high-

resolution O 1s spectra of NiO is presented in Fig. 4d, in which the prominent peaks at 529.0 eV and 530.8 eV are arisen from the Ni–O bond, while the appendant peak at 531.7 eV belongs to the O species in adsorbed H_2O on the surface [49–51]. The high resolution Ni 2p XPS spectra (Fig. 4e) can be resolved into five peaks, which are the typical characteristic peaks of Ni in Ni–O bonds [52,53]. The former peak of Ni 2p_{3/2} located at 853.5 eV and the last peak of Ni 2p_{1/2} at 871.8 eV indicate the existence of Ni^{2+} in NiO [51,54]. The other two satellite peaks at around 860.9 eV and 879.1 eV are induced by shake-up [55]. Besides, the split peak of Ni 2p_{3/2} at 855.3 eV and the O 1s band at 530.8 eV suggest the co-existence of Ni_2O_3 [53]. Furthermore, a slighted shift in the banding energy of C 1s, O 1s and Ni 2p are all observed in the spectra of 40% NiO/ $\text{g-C}_3\text{N}_4$ composite. From the literatures [56,57], a shift of binding energy was attributed to the different electron concentration that caused by electron transfer and interfacial interaction in the formed p-n heterojunction. The results are accordant with the TEM image, XRD and FTIR results discussed above.

N_2 adsorption-desorption was performed to analyze the textural properties of as-prepared catalysts. It can be seen that all samples exhibit the type IV isotherms with a hysteresis loop (Fig. 5a), reflecting the mesoporous structure presented in the composites. The specific surface areas and pore sizes of all samples are summarized in Table 1. It is obvious that the ball-flower like heteroarchitectures could enhance the BET surface area (the maximum is 120.1 m^2/g for 40% NiO/ $\text{g-C}_3\text{N}_4$) greatly in contrast to that of the pure flaky $\text{g-C}_3\text{N}_4$ (64.7 m^2/g) and ball-flower NiO (57.6 m^2/g). The increase of the specific surface area may provide more active sites for reaction. The BJH pore size distributions of $\text{g-C}_3\text{N}_4$, NiO and NiO/ $\text{g-C}_3\text{N}_4$ composites (Fig. 5b) reveal the narrow pore size distribution ranged from 3.6 nm to 4.1 nm.

The optical properties of NiO, $\text{g-C}_3\text{N}_4$, and NiO/ $\text{g-C}_3\text{N}_4$ composites were characterized by UV-vis within the range of 250–800 nm, which

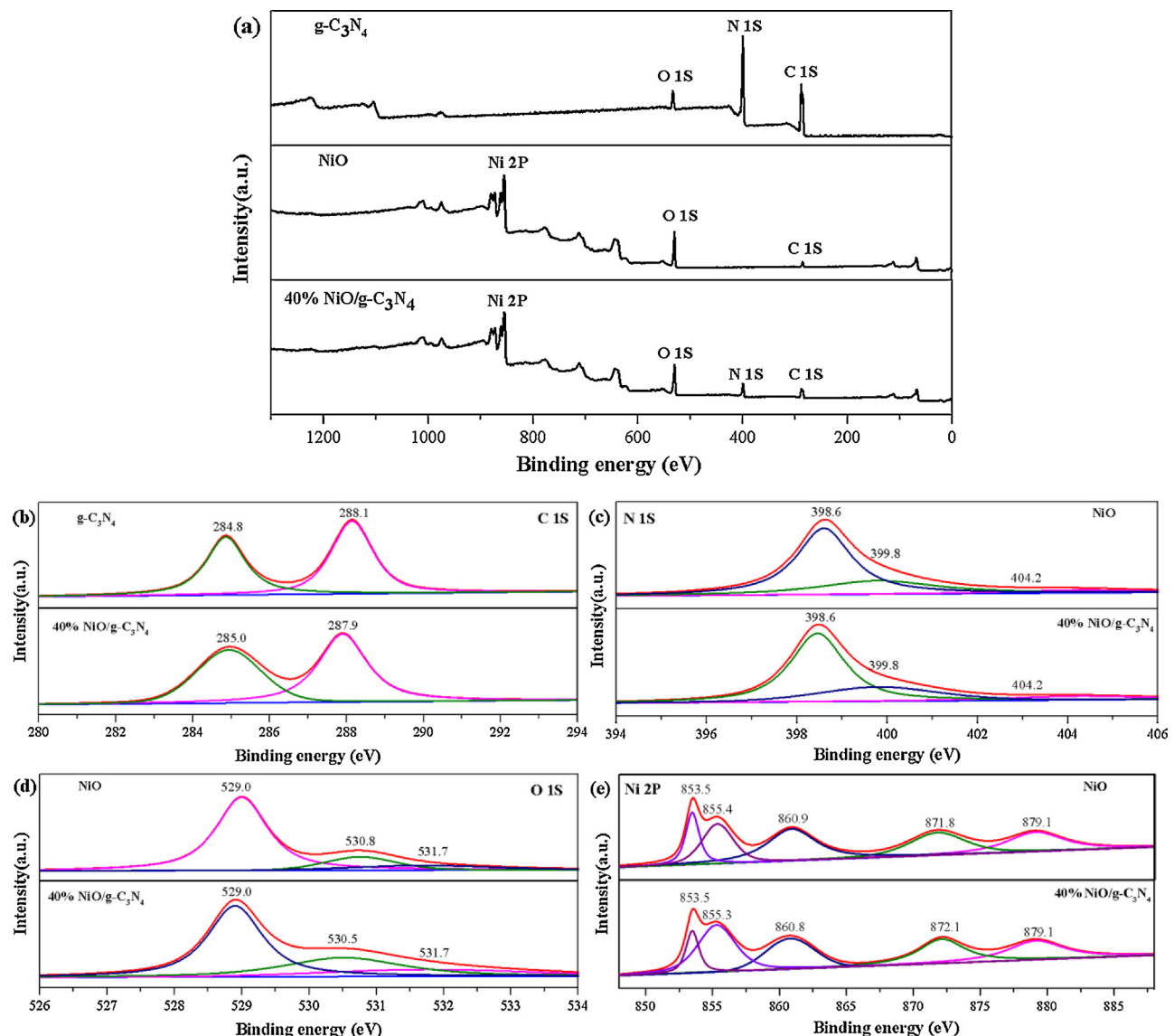


Fig. 4. XPS survey spectra of $\text{g-C}_3\text{N}_4$, NiO and 40% $\text{NiO}/\text{g-C}_3\text{N}_4$ composite (a); high-resolution C 1s (b) and N 1s (c) spectra of $\text{g-C}_3\text{N}_4$ and 40% $\text{NiO}/\text{g-C}_3\text{N}_4$ composite; high-resolution O 1s (d) and Ni 2p (e) spectra of NiO and 40% $\text{NiO}/\text{g-C}_3\text{N}_4$ composite.

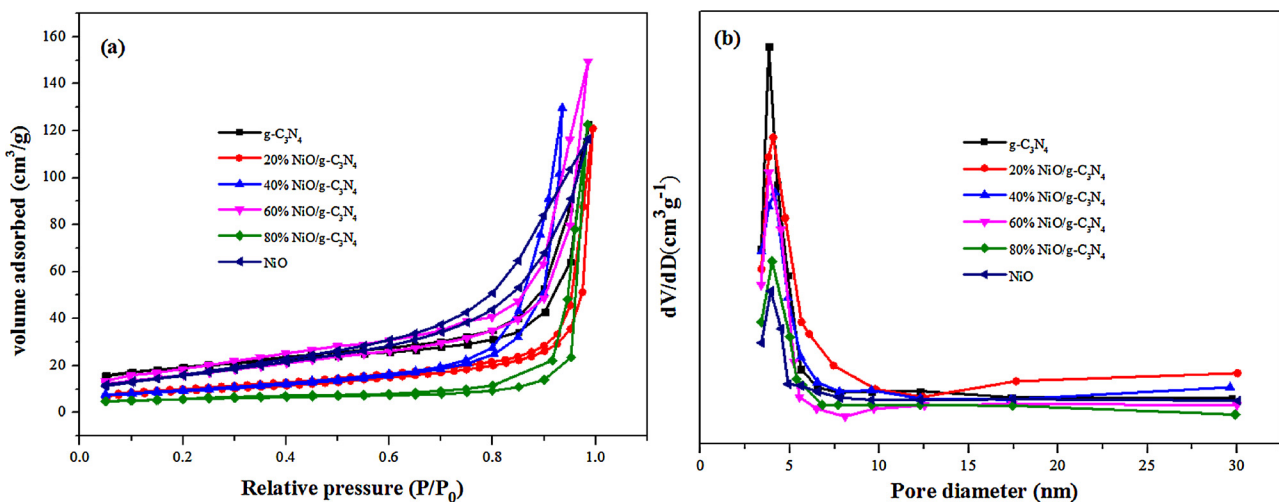


Fig. 5. N_2 adsorption–desorption isotherms and corresponding pore size distribution curves obtained from the desorption branch of the as-prepared catalysts.

Table 1

Textural properties of the pure $\text{g-C}_3\text{N}_4$, pure NiO and NiO/ $\text{g-C}_3\text{N}_4$ composite catalysts.

Samples	S_{BET} (m^2/g)	Pore size (nm)
$\text{g-C}_3\text{N}_4$	64.7	3.829
20% NiO/ $\text{g-C}_3\text{N}_4$	101.8	3.824
40% NiO/ $\text{g-C}_3\text{N}_4$	120.1	3.808
60% NiO/ $\text{g-C}_3\text{N}_4$	108.3	3.819
80% NiO/ $\text{g-C}_3\text{N}_4$	89.2	3.813
NiO	57.6	3.869

were converted from the corresponding diffuse reflectance spectra based on the Kubelka–Munk function. As shown in Fig. 6a, the adsorption edge of pure $\text{g-C}_3\text{N}_4$ at 440 nm is clearly observed and the ball-flower NiO shows a strong adsorption in both the UV and visible-light regions due to its dark green color. For the NiO/ $\text{g-C}_3\text{N}_4$ composites, the adsorption bands attributed to the characteristic adsorption of NiO and $\text{g-C}_3\text{N}_4$ are also detected with a significant enhancement in the visible-light adsorption range (450–800 nm), which may be due to the synergistic effect between NiO and $\text{g-C}_3\text{N}_4$. Furthermore, the adsorption values of NiO/ $\text{g-C}_3\text{N}_4$ samples appear stronger than that of $\text{g-C}_3\text{N}_4$ based on the vertical coordinates, which is helpful to utilize the light adsorption and facilitate the photocatalytic reaction. The band gap of $\text{g-C}_3\text{N}_4$ and NiO were also estimated according to the formula $\alpha h\nu = A(h\nu - E_g)^{n/2}$, where α , $h\nu$, A and E_g represent the adsorption coefficient, Plank's constant, the light frequency, a constant relative to the material and the band gap energy, respectively. What's more, n is dependent on the type of the transition in a semiconductor. With regard to the indirect transition catalyst of $\text{g-C}_3\text{N}_4$ and direct transition catalyst of NiO, n is equal to 4 and 1, respectively. Based on the above mentioned formula, the band gap energy of pure $\text{g-C}_3\text{N}_4$ and NiO are 2.65 eV and 3.3 eV, respectively (Fig. 6b).

In order to further confirm the exact band-edge positions of NiO and $\text{g-C}_3\text{N}_4$, Mott–Schottky method was employed (Fig. 7), the flat-band potentials of NiO and $\text{g-C}_3\text{N}_4$ can be determined by extrapolating to $C^{-2} = 0$ at the frequencies of 500 Hz and 1000 Hz. The C^{-2} in vertical coordinates is a function of electrochemical potentials, where the capacitance C can be obtained from the impedance measurement. The negative slope of NiO in Mott–Schottky curve indicates a p-type NiO (Fig. 7a). Similarly, the positive slope of $\text{g-C}_3\text{N}_4$ suggests the n-type semiconductor characteristics (Fig. 7b). The flat potentials of NiO and $\text{g-C}_3\text{N}_4$ are 0.85 and -0.55 V versus the Ag/AgCl electrode, respectively, which are equal to 1.05 and -0.35 V versus the normal hydrogen electrode (NHE) [58,59]. The inset images of Fig. 7 are the VB

XPS spectra of NiO and $\text{g-C}_3\text{N}_4$. It can be seen that the energy gap between the VB and Fermi level (E_f) is 0.30 and 2.05 eV for NiO and $\text{g-C}_3\text{N}_4$, respectively [60,61], demonstrating that the Fermi level of p-type catalyst is close to the VB while that of n-type sample is located near the CB. It is generally accepted that the value of the flat potentials is approximately equal to that of the Fermi level [62–65]. Consequently, the VB potential for NiO is about 1.35 eV and the VB position for $\text{g-C}_3\text{N}_4$ is equal to 1.70 eV. Furthermore, the CB for NiO and $\text{g-C}_3\text{N}_4$ are calculated to be -1.95 and -0.95 eV respectively based on their band gaps. The diagram of the band energy for NiO and $\text{g-C}_3\text{N}_4$ are displayed in Scheme 1. Therefore, these band alignments of p-type NiO and n-type $\text{g-C}_3\text{N}_4$ meet the requirement for the photocatalytic reduction of CO_2 .

The photocatalytic activities of the as-prepared samples were investigated on CO_2 reduction under visible-light irradiation. The main product is found to be CO while only a trace amount of CH_4 was detected (Fig. S1a) during the reaction process. Moreover, O_2 , as the oxidation product, was also detected in the outlet gases (Fig. S1b). Control experiments were also conducted and no hydrocarbon products are detected without illumination or photocatalyst, which suggests that the CO_2 photocatalytic reduction process is inevitable owing to above factors. Fig. 8a shows the comparison of CO production amount with error bars in the unit time on the as-synthesised samples during the photoreaction. It can be seen that only trace amount of CO is observed for NiO sample. The same phenomena can be seen on $\text{g-C}_3\text{N}_4$, which may be ascribed to the small surface area and rapid recombination rate of electron–hole pairs during the reaction. While the heterojunction formed in the NiO/ $\text{g-C}_3\text{N}_4$ composites, remarkable CO production is obtained surprisingly. The activity improves as the increase of NiO content, which may due to the increase amount of heterojunctions. A maximum CO production amount of $4.17 \mu\text{mol h}^{-1} \text{g}^{-1}$ is achieved on 40% NiO/ $\text{g-C}_3\text{N}_4$ catalyst during 8 h reaction, which is about 2.5 times and 7.6 times as high as pure $\text{g-C}_3\text{N}_4$ and pure NiO, respectively. However, the photocatalytic activity decreased with further increase of NiO content. It may arise from the decrease of reaction active sites with low specific surface area, and the excessive NiO may act as recombination centers for charge carriers during the photocatalytic reduction process [66]. In order to further explore the fact of the above inference, the separation rate of the electron–hole pairs was tested by photoluminescence. As shown in Fig. 8b, a faintest emission peak of NiO is hardly observed, which may originate from the defects or surface oxygen vacancies on NiO [67]. Compared to NiO, an intensive emission peak centered at 450 nm is observed in the spectrum of $\text{g-C}_3\text{N}_4$, implying the faster recombination of electrons and holes. Compared to $\text{g-C}_3\text{N}_4$, the NiO/ $\text{g-C}_3\text{N}_4$ composites exhibit a weaker emission peak in PL spectrum, suggesting the efficient separation of electron–hole pairs due

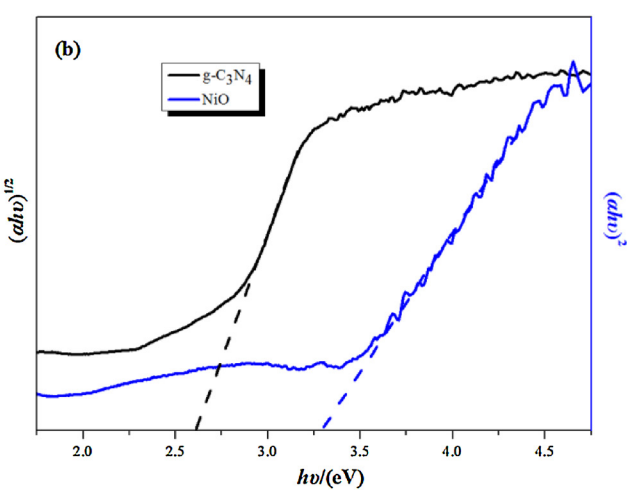
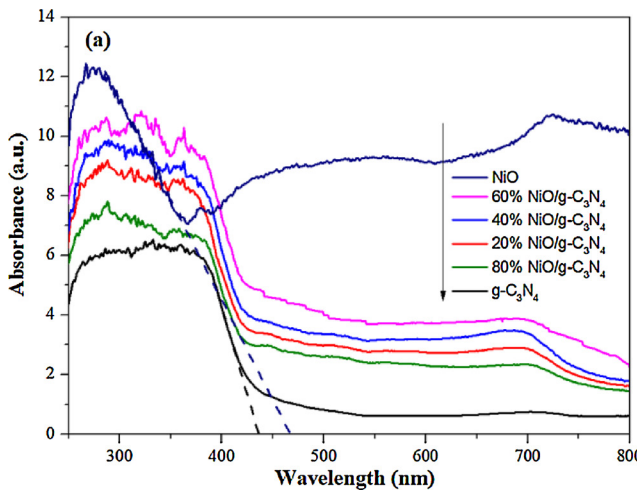


Fig. 6. (a) UV–vis diffuse reflectance spectra for pure $\text{g-C}_3\text{N}_4$, pure NiO, and ball-flower like NiO $\text{g-C}_3\text{N}_4$ heteroarchitectures. (b) The plots of $(\alpha h\nu)^{1/2}$ and $(\alpha h\nu)^2$ versus energy ($h\nu$) for the band gap energies of pure $\text{g-C}_3\text{N}_4$ and pure NiO, respectively.

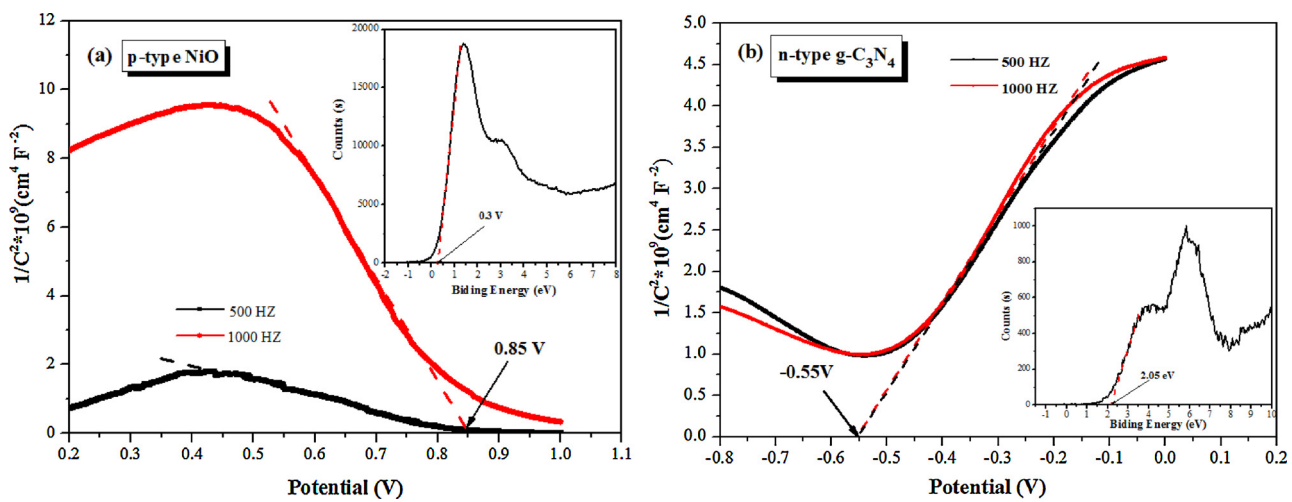
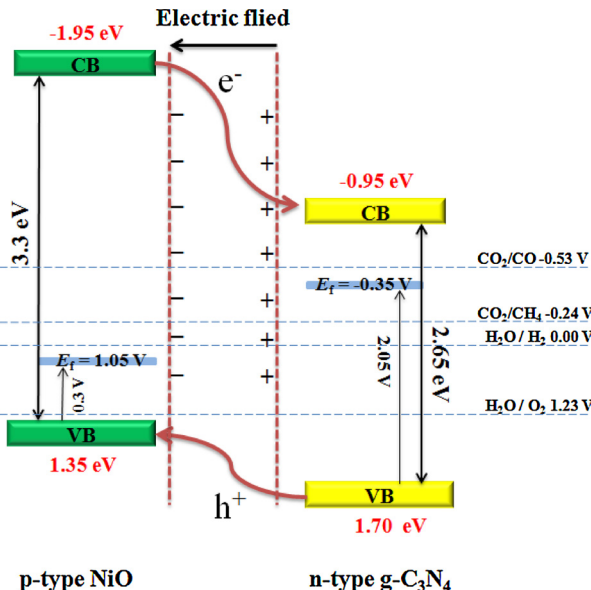


Fig. 7. Mott-Schottky plots and Valence band energy (inset) collected for pure NiO (a) and g-C₃N₄ (b).



Scheme 1. Schematic of band positions of NiO and g-C₃N₄ and CO_2 photoreduction mechanism on NiO/g-C₃N₄ heterojunction composites.

to the formation of NiO/g-C₃N₄ heterojunctions. Noticeably, the 40% NiO/g-C₃N₄ composite possesses the lowest PL intensity among all the NiO/g-C₃N₄ composites. The PL results confirm the p-n junction effect in NiO/g-C₃N₄ heterostructure, which leads to an effective separation of photo-induced charges. Furthermore, in the hope of investigating the photocatalytic stability of the 40% NiO/g-C₃N₄ photocatalyst, three consecutive CO_2 photoreduction cycles were conducted by vacuum treatment every 5 h for 30 min to remove the products. As shown in Fig. 8c, no significant decrease for CO production was observed during the three experimental runs. This indicates a stable performance of 40% NiO/g-C₃N₄ during the photocatalytic reaction.

The excitation and transfer of charge carriers in NiO, g-C₃N₄ and NiO/g-C₃N₄ heterojunction composites were further studied by photo-electrochemical measurements. Fig. 9a shows the photocurrent responses under visible-light irradiation in six on-off cycles. The transient photocurrent results provide more clear evidence on electron transfer efficiency within the formed heterojunctions. A uniform and fast photocurrent response can be observed upon the samples in the light-on and light-off test, indicating the stable photocatalytic activity. The pure NiO exhibits rapidly increased photocurrent as the light on while the photocurrent intensity decreases with an evident delay as the light off.

This is owing to the gradual release of electrons from the doping channels [68]. The pristine g-C₃N₄ presents a quickly increased current once the light is on and a sharply decline once the light is off. It may derive from the electron trapping and releasing mediated by surface defects [69]. The photocurrent curve feature for NiO/g-C₃N₄ heterojunctions indicates a long balance process when light is turned on or turned off, implying charge carriers experience a long distance during their migration in the heterojunction. As expected, 40% NiO/g-C₃N₄ heterostructured composite with the photocurrent density at $4.1 \mu\text{A cm}^{-2}$, exhibits the highest photocurrent intensity among the test materials, indicating the charge transfer with high-efficiency. To verify this assumption, EIS experiment was also carried out. As shown in Fig. 9b, the semicircular Nyquist plots for the tested samples were obtained. Compared with NiO and g-C₃N₄, the smallest semicircle diameter was observed in 40% NiO/g-C₃N₄ composite, suggesting the accelerated electron transfer in this heterostructured composite, which is in good accordance with its photocatalytic activity as shown before [70].

Based on the abovementioned analysis, the possible reaction mechanism on p-n heterojunctions with excellent photocatalytic performance is discussed in Scheme 1. When p-type NiO and n-type g-C₃N₄ are connected closely, the electrons in n-type g-C₃N₄ transfer to p-type NiO, leading to a positive charge, meanwhile the holes in NiO transfer to g-C₃N₄, generating a negative charge. Consequently, the space charge region called internal electric field is established when the electron and hole accumulate to an equilibrium. Under light irradiation, the electrons in NiO flow into the positive region and the holes move into negative region in the effect of internal electric field. Thus, the holes on the VB of NiO are trapped by H_2O to generate protons and O_2 . Meanwhile, the electrons on the CB of g-C₃N₄ react with CO_2 to produce CO selectively. Obviously, the photogenerated electron-hole pairs will be effectively separated by the formed junction, resulting in a significantly enhanced photocatalytic activity. Furthermore, it has been recognized that the p-type NiO with the existed Ni^{3+} on its surface could increase the absorption of visible light and reduce the electric resistance of NiO, which benefits the photocatalytic reduction of CO_2 [28,50]. In addition, the photocatalysts are selective to produce CO while only trace of CH_4 molecules were formed, which may be due to the following reasons: (1) active sites on g-C₃N₄ for CO_2 reduction reaction might be covered by the formed CO and/or intermediate products (C), resulting in the insufficient electrons contacted with CO_2 molecules to produce CH_4 [71–73]; (2) the generated hydrogen consume lots of electrons (Table S1), which is competitive to produce CH_4 . Moreover, the ball-flower structure with larger specific surface area that can provide massive active sites is also one of the main reasons for

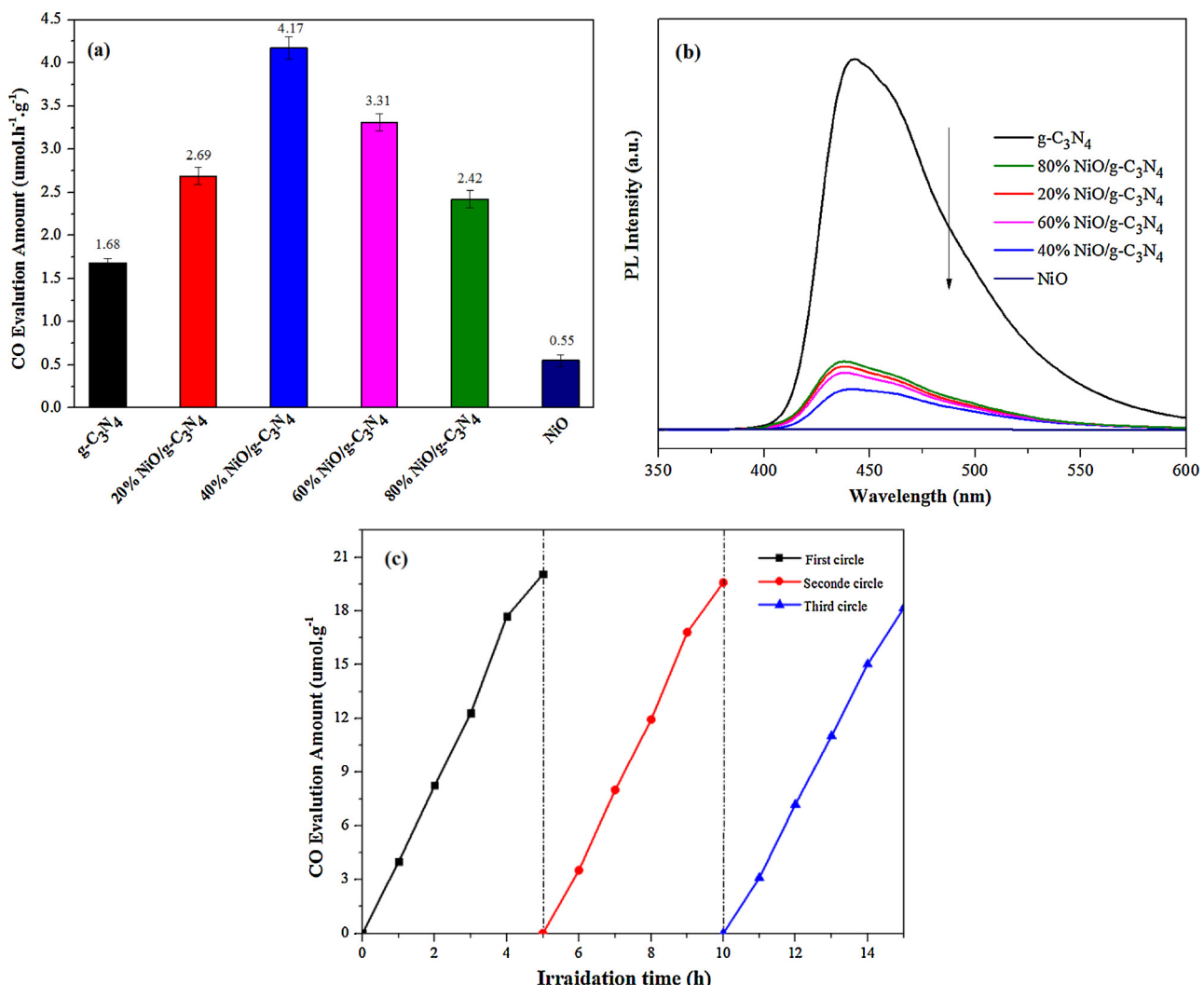


Fig. 8. (a) CO evolution amount in the unit time (b) PL spectra of pure NiO, pure g-C₃N₄ and NiO/g-C₃N₄ heterojunctions and (c) repeatability of photocatalytic CO evolution via the 40% NiO/g-C₃N₄ photocatalyst.

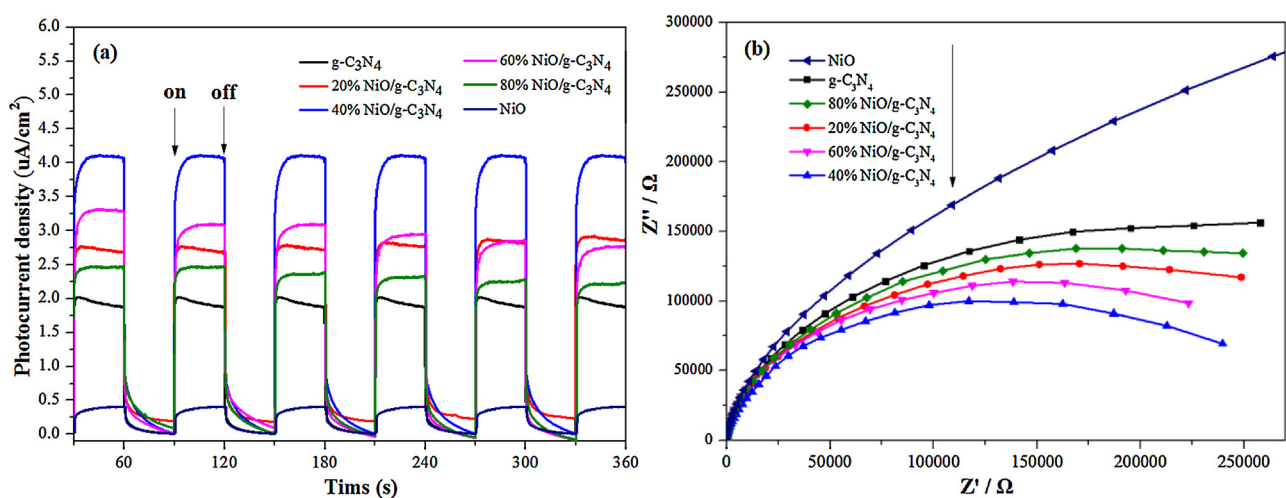


Fig. 9. (a) Transient photocurrent density and (b) electrochemical impedance spectra of pure NiO, pure g-C₃N₄ and NiO/g-C₃N₄ composites.

the superior photocatalytic activity.

4. Conclusions

In summary, the ball-flower $\text{NiO}/\text{g-C}_3\text{N}_4$ heterojunctions were successfully synthesized via a hydrothermal doping process combined with the subsequent calcination method. The obtained 40% $\text{NiO}/\text{g-C}_3\text{N}_4$ composite manifests the highest photocatalytic activity in reduction CO_2 to CO , which is 2.5 and 7.6 times as high as pure $\text{g-C}_3\text{N}_4$ and pure NiO , respectively. The remarkable improvement of photocatalytic activity is mainly owing to the efficient separation of charge carriers resulted from the perfect band matching and internal charge transfer within the p-n junction. It is noteworthy that the high specific surface area and the strong visible light response also contribute to its high photocatalytic reduction performance. This study paves a prospective p-n heterojunction photocatalysts with strong visible-light response, which can further improve the photocatalytic performance of $\text{g-C}_3\text{N}_4$ catalyst.

Acknowledgments

This work was supported by the Natural Science Foundation of China (21546014) and the Natural Science Foundation of Shanghai, China (14ZR1417800).

Appendix A. Supplementary data

Supplementary material related to this article can be found, in the online version, at doi:<https://doi.org/10.1016/j.apcatb.2018.06.042>.

References

- [1] M.R. Hoffmann, S.T. Martin, W. Choi, D.W. Bahnemann, *Chem. Rev.* 95 (1995) 69–96.
- [2] T. Inoue, A. Fujishima, S. Konishi, K. Honda, *Nature* 277 (1979) 637–638.
- [3] A.J. Morris, G.J. Meyer, E. Fujita, *Acc. Chem. Res.* 42 (2009) 1983–1994.
- [4] A. Corma, H. Garcia, *J. Catal.* 308 (2013) 168–175.
- [5] X. Wang, K. Maeda, A. Thomas, K. Takanabe, G. Xin, J. Carlsson, K. Domen, M. Antonietti, *Nat. Mater.* 8 (2009) 76–80.
- [6] J. Qin, S. Wang, H. Ren, Y. Hou, X. Wang, *Appl. Catal. B: Environ.* 179 (2015) 1–8.
- [7] Y. Zhang, T. Mori, J. Ye, M. Antonietti, *J. Am. Chem. Soc.* 132 (2010) 6294–6295.
- [8] Q. Xiang, J. Yu, M. Jaroniec, *J. Phys. Chem. C* 115 (2011) 7355–7363.
- [9] Y. Guo, S. Chu, S. Yan, Y. Wang, Z. Zou, *Chem. Commun.* 46 (2010) 7325–7327.
- [10] G. Gao, Y. Jiao, E.R. Waclawik, A. Du, J. *Am. Chem. Soc.* 138 (2016) 6292–6297.
- [11] X. Chen, J. Zhang, X. Fu, M. Antonietti, X. Wang, *J. Am. Chem. Soc.* 131 (2009) 11658–11659.
- [12] K. Wang, Q. Li, B. Liu, B. Cheng, W. Ho, J. Yu, *Appl. Catal. B: Environ.* 176–177 (2015) 44–52.
- [13] J. Tang, W. Zhou, R. Guo, C. Huang, W. Pan, *Catal. Commun.* 107 (2018) 92–95.
- [14] D. Zheng, C. Huang, X. Wang, *Nanoscale* 7 (2015) 465–470.
- [15] X. Bai, J. Li, C. Cao, S. Hussain, *Mater. Lett.* 65 (2011) 1101–1104.
- [16] X. Zhou, B. Jin, L. Li, F. Peng, H. Wang, H. Yu, Y. Fang, *J. Mater. Chem.* 22 (2012) 17900–17905.
- [17] J. Zhao, Z. Ji, X. Shen, H. Zhou, L. Ma, *Ceram. Int.* 41 (2015) 5600–5606.
- [18] M. Li, L. Zhang, X. Fan, M. Wu, M. Wang, R. Cheng, L. Zhang, H. Yao, J. Shi, *Appl. Catal. B: Environ.* 201 (2017) 629–635.
- [19] M. Li, L. Zhang, M. Wu, Y. Du, X. Fan, M. Wang, L. Zhang, Q. Kong, J. Shi, *Nano Energy* 19 (2016) 145–155.
- [20] M. Wang, M. Shen, L. Zhang, J. Tian, X. Jin, Y. Zhou, J. Shi, *Carbon* 120 (2017) 23–31.
- [21] F. Guo, W. Shi, H. Wang, M. Han, H. Li, H. Huang, Y. Liu, Z. Kang, *Catal. Sci. Technol.* 7 (2017) 3325–3331.
- [22] G. Natu, P. Hasin, Z. Huang, Z. Ji, M. He, Y. Wu, *ACS Appl. Mater. Interfaces* 4 (2012) 5922–5929.
- [23] A. Nattestad, A.J. Mozer, M.K.R. Fischer, Y.B. Cheng, A. Mishra, P. Bauerle, *Nat. Mater.* 9 (2010) 31–35.
- [24] F. Odobel, Y. Pellegrin, *J. Phys. Chem. Lett.* 4 (2013) 2551–2564.
- [25] S.E. Habas, H.A.S. Platt, M.F.A.M.V. Hest, D.S. Ginley, *Chem. Rev.* 110 (2010) 6571–6594.
- [26] X. Wan, M. Yuan, S.L. Tie, S. Lan, *J. South China Normal Univ.* 277 (2013) 40–46.
- [27] B.A. Nail, J.M. Fields, J. Zhao, J. Wang, M.J. Greaney, R.L. Brutchey, F.E. Osterloh, *ACS Nano* 9 (2015) 5135–5142.
- [28] L. Sim, K. Ng, S. Ibrahim, P. Saravanan, *Int. J. Photoenergy* 2013 (2013) 749–756.
- [29] K. Klier, K. Kuchynka, *J. Catal.* 6 (1966) 62.
- [30] M. Breysse, B. Claudel, L. Faure, M. Guenin, R.J.J. Williams, *J. Catal.* 45 (1976) 137.
- [31] C. Hu, H. Teng, *J. Catal.* 272 (2010) 1–8.
- [32] C. Chen, C. Liao, K. Hsu, Y. Wu, J.C.S. Wu, *Catal. Commun.* 12 (2011) 1307–1310.
- [33] B. Sun, G. Zhou, T. Gao, H. Zhang, H. Yua, *Appl. Surf. Sci.* 364 (2016) 322–331.
- [34] T. Sreethawong, Y. Suzuki, S. Yoshikawa, *Int. J. Hydrogen Energy* 30 (2005) 1053–1062.
- [35] M. Xiao, Y. Lu, Y. Li, H. Song, L. Zhu, Z. Ye, *RSC Adv.* 4 (2014) 34649–34653.
- [36] Z. Khan, M. Khannam, N. Vinothkumar, M. De, M. Qureshi, *J. Mater. Chem.* 22 (2012) 12090–12095.
- [37] Z. Zhang, C. Shao, X. Li, C. Wang, M. Zhang, Y. Liu, *ACS Appl. Mater. Interfaces* 2 (2010) 2915–2923.
- [38] A. Nattestad, A.J. Mozer, M.K.R. Fischer, Y.B. Cheng, A. Mishra, P. Bauerle, *Nat. Mater.* 9 (2010) 31–35.
- [39] X.H. Li, J.S. Chen, X. Wang, J. Sun, M. Antonietti, *J. Am. Chem. Soc.* 133 (2011) 8074–8077.
- [40] F. Guo, W. Shi, X. Lin, G. Che, *J. Phys. Chem. Solids* 75 (2014) 1217–1222.
- [41] W. Shi, F. Guo, J. Chen, G. Che, X. Lin, *J. Alloys Compd.* 612 (2014) 143–148.
- [42] X. Lin, B. Wei, X. Zhang, M. Song, S. Yu, Z. Gao, H. Zhai, L. Zhao, G. Che, *Sep. Purif. Technol.* 169 (2016) 9–16.
- [43] S. Selvarajan, A. Suganthi, M. Rajarajanc, *Ultrason. Sonochem.* 41 (2018) 651–660.
- [44] M. El-Kemary, N. Nagy, I. El-Mehasseb, *Mater. Sci. Semi. Proc.* 16 (2013) 1747–1752.
- [45] Y. Yu, L. Guo, H. Cao, Y. Lv, E. Wang, Y. Cao, *Sep. Purif. Technol.* 142 (2015) 14–17.
- [46] Y. Li, H. Zhang, P. Liu, D. Wang, H. Zhao, *Small* 9 (2013) 3336–3344.
- [47] C. Zhang, R. Hao, H. Liao, Y. Hou, *Nano Energy* 2 (2013) 88–97.
- [48] S. Thaweesak, M. Lyu, P. Peerakiatkhajohn, T. Butburee, B. Luo, H. Chen, L. Wang, *Appl. Catal. B: Environ.* 202 (2017) 184–190.
- [49] V.P. Santos, M.F.R. Pereira, J.J.M. Órfão, J.L. Figueiredo, *Appl. Catal. B: Environ.* 99 (2010) 353–363.
- [50] J. Guo, W. Fu, H. Yang, Q. Yu, W. Zhao, X. Zhou, Y. Sui, J. Ding, Y. Li, S. Cheng, M. Li, *J. Phys. D: Appl. Phys.* 43 (2010) 245202.
- [51] Y. Zhang, J. Wang, P. Wan, J. Ye, S. Hussain, H. Wei, D. Hou, *Mater. Lett.* 177 (2016) 71–75.
- [52] W. Dai, X. Pan, S. Chen, C. Chen, Z. Wen, H. Zhang, Z. Ye, *J. Mater. Chem. C* 2 (2014) 4606–4614.
- [53] K.S. Kim, R.E. Davis, *J. Electron. Spectrosc. Relat. Phenom.* 1 (1972) 251–258.
- [54] J. Xu, L. Li, F. He, R.C. Lv, P.P. Yang, *Electrochim. Acta* 148 (2014) 211–219.
- [55] W. Dai, X. Pan, S. Chen, C. Chen, Z. Wen, H. Zhang, Z. Ye, *J. Mater. Chem. C* 2 (2014) 4606–4614.
- [56] Z. Huang, Q. Sun, K. Lv, Z. Zhang, M. Li, B. Li, *Appl. Catal. B: Environ.* 164 (2015) 420–427.
- [57] M. Lu, Z. Pei, S. Weng, W. Feng, Z. Fang, Z. Zheng, M. Huang, P. Liu, *Phys. Chem. Chem. Phys.* 16 (2014) 21280–21288.
- [58] S.J. Hong, S. Lee, J.S. Jang, J.S. Lee, *Energy Environ. Sci.* 4 (2011) 1781–1787.
- [59] K. Sayama, A. Nomura, T. Arai, T. Sugita, R. Abe, M. Yanagida, T. Oi, Y. Iwasaki, Y. Abe, H. Sugihara, *J. Phys. Chem. B* 110 (2006) 11352–11360.
- [60] W. Luo, Z. Li, X. Jiang, T. Yu, L. Liu, X. Chen, J. Ye, Z. Zou, *Phys. Chem. Chem. Phys. CCP* 10 (2008) 6717–6723.
- [61] C. Liu, Y. Zhang, F. Dong, A.H. Reshak, L. Ye, N. Pinna, C. Zeng, T. Zhang, H. Huang, *Appl. Catal. B: Environ.* 203 (2017) 465–474.
- [62] H. Li, H. Yu, X. Quan, S. Chen, Y. Zhang, *ACS. Appl. Mater. Interfaces* 8 (2016) 2111–2119.
- [63] Y. Bai, L. Ye, T. Chen, L. Wang, X. Shi, X. Zhang, D. Chen, *ACS. Appl. Mater. Interfaces* 8 (2016) 27661–27668.
- [64] E. Gao, W. Wang, M. Shang, J. Xu, *Phys. Chem. Chem. Phys.* 13 (2011) 2887–2893.
- [65] D.E. Scaife, *Sol. Energy* 25 (1980) 41–54.
- [66] X. Chen, S. Shen, L. Guo, S. Mao, *Chem. Rev.* 110 (2010) 6503–6570.
- [67] L. Jing, Y. Qu, B. Wang, S. Li, B. Jiang, L. Yang, W. Fu, H. Fu, J. Sun, *Sol. Energy Mater. Sol. Cells* 90 (2006) 1773–1787.
- [68] S. Cao, Q. Huang, B. Zhu, J. Yu, *J. Power Sources* 351 (2017) 151–159.
- [69] D. Jiang, W. Wang, S. Sun, L. Zhang, Y. Zheng, *ACS Catal.* 5 (2015) 613–621.
- [70] S. Sun, W. Wang, L. Zhang, J. Phys. Chem. C 117 (2013) 9113–9120.
- [71] M. Tahir, B. Tahir, *Appl. Surf. Sci.* 377 (2016) 244–252.
- [72] I.H. Tseng, W.C. Chang, J.C.S. Wu, *Appl. Catal. B: Environ.* 37 (2002) 37–48.
- [73] L. Li, B. Cheng, Y. Wang, J. Yu, *J. Solid State Chem.* 449 (2015) 115–121.